

## 23. COSMIC MICROWAVE BACKGROUND

Revised August 2009 by D. Scott (University of British Columbia) and G.F. Smoot (UCB/LBNL).

### 23.1. Introduction

The energy content in radiation from beyond our Galaxy is dominated by the Cosmic Microwave Background (CMB), discovered in 1965 [1]. The spectrum of the CMB is well described by a blackbody function with  $T = 2.725$  K. This spectral form is one of the main pillars of the hot Big Bang model for the early Universe. The lack of any observed deviations from a blackbody spectrum constrains physical processes over cosmic history at redshifts  $z \lesssim 10^7$  (see earlier versions of this review). All viable cosmological models predict a very nearly Planckian spectrum inside the current observational limits.

Another observable quantity inherent in the CMB is the variation in temperature (or intensity) from one part of the microwave sky to another [2]. Since the first detection of these anisotropies by the *COBE* satellite [3], there has been intense activity to map the sky at increasing levels of sensitivity and angular resolution by ground-based and balloon-borne measurements. These were joined in 2003 by the first results from NASA's Wilkinson Microwave Anisotropy Probe (*WMAP*) [4], which were improved upon by analysis of the 3 year and 5 year *WMAP* data [5,6]. Together these observations have led to a stunning confirmation of the 'Standard Model of Cosmology.' In combination with other astrophysical data, the CMB anisotropy measurements place quite precise constraints on a number of cosmological parameters, and have launched us into an era of precision cosmology. This is expected to continue with the improved capabilities of the *Planck* satellite.

### 23.2. Description of CMB Anisotropies

Observations show that the CMB contains anisotropies at the  $10^{-5}$  level, over a wide range of angular scales. These anisotropies are usually expressed by using a spherical harmonic expansion of the CMB sky:

$$T(\theta, \phi) = \sum_{\ell m} a_{\ell m} Y_{\ell m}(\theta, \phi).$$

The vast majority of the cosmological information is contained in the temperature 2-point function, *i.e.*, the variance as a function only of angular separation, since we notice no preferred direction. Equivalently, the power per unit  $\ln \ell$  is  $\ell \sum_m |a_{\ell m}|^2 / 4\pi$ .

#### 23.2.1. The Monopole :

The CMB has a mean temperature of  $T_\gamma = 2.725 \pm 0.001$  K ( $1\sigma$ ) [7], which can be considered as the monopole component of CMB maps,  $a_{00}$ . Since all mapping experiments involve difference measurements, they are insensitive to this average level. Monopole measurements can only be made with absolute temperature devices, such as the FIRAS instrument on the *COBE* satellite [7]. Such measurements of the spectrum are consistent with a blackbody distribution over more than three decades in frequency (with some recent evidence for deviation at low frequencies [8]). A blackbody of the measured temperature corresponds to  $n_\gamma = (2\zeta(3)/\pi^2) T_\gamma^3 \simeq 411 \text{ cm}^{-3}$  and  $\rho_\gamma = (\pi^2/15) T_\gamma^4 \simeq 4.64 \times 10^{-34} \text{ g cm}^{-3} \simeq 0.260 \text{ eV cm}^{-3}$ .

#### 23.2.2. The Dipole :

The largest anisotropy is in the  $\ell = 1$  (dipole) first spherical harmonic, with amplitude  $3.355 \pm 0.008$  mK [6]. The dipole is interpreted to be the result of the Doppler shift caused by the solar system motion relative to the nearly isotropic blackbody field, as confirmed by measurements of the radial velocities of local galaxies [9]. The motion of an observer with velocity  $\beta \equiv v/c$  relative to an isotropic Planckian radiation field of temperature  $T_0$  produces a Doppler-shifted temperature pattern

$$\begin{aligned} T(\theta) &= T_0 (1 - \beta^2)^{1/2} / (1 - \beta \cos \theta) \\ &\simeq T_0 \left( 1 + \beta \cos \theta + \left( \beta^2/2 \right) \cos 2\theta + O(\beta^3) \right). \end{aligned}$$

At every point in the sky, one observes a blackbody spectrum, with temperature  $T(\theta)$ . The spectrum of the dipole is the differential of a blackbody spectrum, as confirmed by Ref. 10.

The implied velocity for the solar system barycenter is  $v = 369.0 \pm 0.9 \text{ km s}^{-1}$ , assuming a value  $T_0 = T_\gamma$ , towards  $(\ell, b) = (263.99^\circ \pm 0.14^\circ, 48.26^\circ \pm 0.03^\circ)$  [6,11]. Such a solar system motion implies a velocity for the Galaxy and the Local Group of galaxies relative to the CMB. The derived value is  $v_{\text{LG}} = 627 \pm 22 \text{ km s}^{-1}$  towards  $(\ell, b) = (276^\circ \pm 3^\circ, 30^\circ \pm 3^\circ)$ , where most of the error comes from uncertainty in the velocity of the solar system relative to the Local Group.

The dipole is a frame-dependent quantity, and one can thus determine the 'absolute rest frame' as that in which the CMB dipole would be zero. Our velocity relative to the Local Group, as well as the velocity of the Earth around the Sun, and any velocity of the receiver relative to the Earth, is normally removed for the purposes of CMB anisotropy study.

#### 23.2.3. Higher-Order Multipoles :

The variations in the CMB temperature maps at higher multipoles ( $\ell \geq 2$ ) are interpreted as being mostly the result of perturbations in the density of the early Universe, manifesting themselves at the epoch of the last scattering of the CMB photons. In the hot Big Bang picture, the expansion of the Universe cools the plasma so that by a redshift  $z \simeq 1100$  (with little dependence on the details of the model), the hydrogen and helium nuclei can bind electrons into neutral atoms, a process usually referred to as recombination [12]. Before this epoch, the CMB photons are tightly coupled to the baryons, while afterwards they can freely stream towards us.

Theoretical models generally predict that the  $a_{\ell m}$  modes are Gaussian random fields to high precision, *e.g.*, standard slow-roll inflation's non-Gaussian contribution is expected to be one or two orders of magnitude below current observational limits [13]. Although non-Gaussianity of various forms is possible in early Universe models, tests show that Gaussianity is an extremely good simplifying approximation [14], with only some relatively weak indications of non-Gaussianity or statistical anisotropy at large scales. Such signatures found in existing *WMAP* data are generally considered to be subtle foreground or instrumental artefacts [15,16].

A statistically isotropic sky means that all  $m$ s are equivalent, *i.e.*, there is no preferred axis. Together with the assumption of Gaussian statistics, the variance of the temperature field (or equivalently the power spectrum in  $\ell$ ) then fully characterizes the anisotropies. The power summed over all  $m$ s at each  $\ell$  is  $(2\ell + 1)C_\ell / (4\pi)$ , where  $C_\ell \equiv \langle |a_{\ell m}|^2 \rangle$ . Thus averages of  $a_{\ell m}$ s over  $m$  can be used as estimators of the  $C_\ell$ s to constrain their expectation values, which are the quantities predicted by a theoretical model. For an idealized full-sky observation, the variance of each measured  $C_\ell$  (*i.e.*, the variance of the variance) is  $[2/(2\ell + 1)]C_\ell^2$ . This sampling uncertainty (known as 'cosmic variance') comes about because each  $C_\ell$  is  $\chi^2$  distributed with  $(2\ell + 1)$  degrees of freedom for our observable volume of the Universe. For fractional sky coverage,  $f_{\text{sky}}$ , this variance is increased by  $1/f_{\text{sky}}$  and the modes become partially correlated.

It is important to understand that theories predict the expectation value of the power spectrum, whereas our sky is a single realization. Hence the cosmic variance is an unavoidable source of uncertainty when constraining models; it dominates the scatter at lower  $\ell$ s, while the effects of instrumental noise and resolution dominate at higher  $\ell$ s [17].

#### 23.2.4. Angular Resolution and Binning :

There is no one-to-one conversion between multipole  $\ell$  and the angle subtended by a particular spatial scale projected onto the sky. However, a single spherical harmonic  $Y_{\ell m}$  corresponds to angular variations of  $\theta \sim \pi/\ell$ . CMB maps contain anisotropy information from the size of the map (or in practice some fraction of that size) down to the beam-size of the instrument,  $\sigma$ . One can think of the effect of a Gaussian beam as rolling off the power spectrum with the function  $e^{-\ell(\ell+1)\sigma^2}$ .

For less than full sky coverage, the  $\ell$  modes become correlated. Hence, experimental results are usually quoted as a series of 'band powers', defined as estimators of  $\ell(\ell + 1)C_\ell / 2\pi$  over different ranges of  $\ell$ . Because of the strong foreground signals in the Galactic Plane, even 'all-sky' surveys, such as *COBE* and *WMAP* involve a cut sky. The amount of binning required to obtain uncorrelated estimates of power also depends on the map size.

### 23.3. Cosmological Parameters

The current ‘Standard Model’ of cosmology contains around 10 free parameters (see The Cosmological Parameters—Sec. 21 of this *Review*). The basic framework is the Friedmann-Robertson-Walker (FRW) metric (*i.e.*, a universe that is approximately homogeneous and isotropic on large scales), with density perturbations laid down at early times and evolving into today’s structures (see Big-Bang cosmology—Sec. 19 of this *Review*). The most general possible set of density perturbations is a linear combination of an adiabatic density perturbation and some isocurvature perturbations. Adiabatic means that there is no change to the entropy per particle for each species, *i.e.*,  $\delta\rho/\rho$  for matter is  $(3/4)\delta\rho/\rho$  for radiation. Isocurvature means that the set of individual density perturbations adds to zero, for example, matter perturbations compensate radiation perturbations so that the total energy density remains unperturbed, *i.e.*,  $\delta\rho$  for matter is  $-\delta\rho$  for radiation. These different modes give rise to distinct (temporal) phases during growth, with those of the adiabatic scenario being strongly preferred by the data. Models that generate mainly isocurvature type perturbations (such as most topological defect scenarios) are no longer considered to be viable. However, an admixture of the adiabatic mode with up to about 10% isocurvature contribution is still allowed [18].

Within the adiabatic family of models, there is, in principle, a free function describing how the comoving curvature perturbations,  $\mathcal{R}(\mathbf{x}, t)$ , vary with length scale. The great virtue of  $\mathcal{R}$  is that it is constant for a purely adiabatic perturbation. There are physical reasons to anticipate that the variance of these perturbations will be described well by a power-law in scale, *i.e.*, in Fourier space  $\langle |\mathcal{R}|_k^2 \rangle \propto k^{n-4}$ , where  $k$  is wavenumber and  $n$  is the usual definition of spectral index. So-called ‘scale-invariant’ initial conditions (meaning gravitational potential fluctuations which are independent of  $k$ ) correspond to  $n = 1$ . In inflationary models [19], perturbations are generated by quantum fluctuations, which are set by the energy scale of inflation, together with the slope and higher derivatives of the inflationary potential. One generally expects that the Taylor series expansion of  $\ln \mathcal{R}_k(\ln k)$  has terms of steadily decreasing size. For the simplest models, there are thus 2 parameters describing the initial conditions for density perturbations: the amplitude and slope of the power spectrum. These can be explicitly defined, for example, through:

$$\Delta_{\mathcal{R}}^2 \equiv \left\langle |\mathcal{R}|_k^2 \right\rangle = A (k/k_0)^{n-1},$$

with  $A \equiv \Delta_{\mathcal{R}}^2(k_0)$  and  $k_0 = 0.002 \text{ Mpc}^{-1}$ , say. There are many other equally valid definitions of the amplitude parameter (see also Sec. 19 and Sec. 21 of this *Review*), and we caution that the relationships between some of them can be cosmology-dependent. In ‘slow roll’ inflationary models, this normalization is proportional to the combination  $V^3/(V')^2$ , for the inflationary potential  $V(\phi)$ . The slope  $n$  also involves  $V''$ , and so the combination of  $A$  and  $n$  can, in principle, constrain potentials.

Inflation generates tensor (gravitational wave) modes, as well as scalar (density perturbation) modes. This fact introduces another parameter, measuring the amplitude of a possible tensor component, or equivalently the ratio of the tensor to scalar contributions. The tensor amplitude is  $A_T \propto V$ , and thus one expects a larger gravitational wave contribution in models where inflation happens at higher energies. The tensor power spectrum also has a slope, often denoted  $n_T$ , but since this seems unlikely to be measured in the near future, it is sufficient for now to focus only on the amplitude of the gravitational wave component. It is most common to define the tensor contribution through  $r$ , the ratio of tensor to scalar perturbation spectra at some small value of  $k$  (although sometimes it is defined in terms of the ratio of contributions at  $\ell = 2$ ). Different inflationary potentials will lead to different predictions, *e.g.*, for  $\lambda\phi^4$  inflation with 50 e-folds,  $r = 0.32$ , and for  $m^2\phi^2$  inflation  $r \simeq 0.15$ , while other models can have arbitrarily small values of  $r$ . In any case, whatever the specific definition, and whether they come from inflation or something else, the ‘initial conditions’ give rise to a minimum of 3 parameters:  $A$ ,  $n$ , and  $r$ .

The background cosmology requires an expansion parameter (the Hubble Constant,  $H_0$ , often represented through  $H_0 = 100 h \text{ km s}^{-1} \text{ Mpc}^{-1}$ ) and several parameters to describe the matter and energy content of the Universe. These are usually given in terms

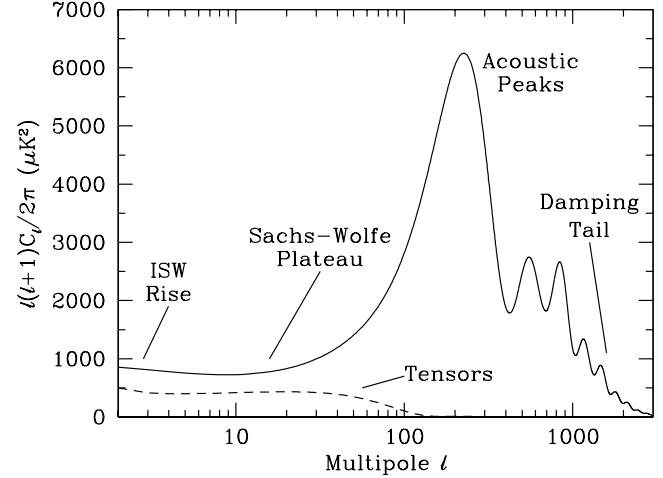


**Figure 23.1:** The theoretical CMB anisotropy power spectrum, using a standard  $\Lambda$ CDM model from CMBFAST. The  $x$ -axis is logarithmic here. The regions, each covering roughly a decade in  $\ell$ , are labeled as in the text: the ISW rise; Sachs-Wolfe plateau; acoustic peaks; and damping tail. Also shown is the shape of the tensor (gravitational wave) contribution, with an arbitrary normalization.

of the critical density, *i.e.*, for species ‘ $x$ ’,  $\Omega_x \equiv \rho_x/\rho_{\text{crit}}$ , where  $\rho_{\text{crit}} \equiv 3H_0^2/8\pi G$ . Since physical densities  $\rho_x \propto \Omega_x h^2 \equiv \omega_x$  are what govern the physics of the CMB anisotropies, it is these  $\omega$ s that are best constrained by CMB data. In particular CMB observations constrain  $\Omega_b h^2$  for baryons and  $\Omega_m h^2$  for baryons plus Cold Dark Matter.

The contribution of a cosmological constant  $\Lambda$  (or other form of Dark Energy) is usually included via a parameter which quantifies the curvature,  $\Omega_K \equiv 1 - \Omega_{\text{tot}}$ , where  $\Omega_{\text{tot}} = \Omega_m + \Omega_\Lambda$ . The radiation content, while in principle a free parameter, is precisely enough determined by the measurement of  $T_\gamma$ , and makes a  $< 10^{-4}$  contribution to  $\Omega_{\text{tot}}$  today.

The main effect of astrophysical processes on the  $C_\ell$ s comes through reionization. The Universe became reionized at some redshift  $z_i$ , long after recombination, affecting the CMB through the integrated Thomson scattering optical depth:

$$\tau = \int_0^{z_i} \sigma_T n_e(z) \frac{dt}{dz} dz,$$

where  $\sigma_T$  is the Thomson cross-section,  $n_e(z)$  is the number density of free electrons (which depends on astrophysics), and  $dt/dz$  is fixed by the background cosmology. In principle,  $\tau$  can be determined from the small-scale matter power spectrum, together with the physics of structure formation and feedback processes. However, this is a sufficiently intricate calculation that  $\tau$  needs to be considered as a free parameter.

Thus, we have 8 basic cosmological parameters:  $A$ ,  $n$ ,  $r$ ,  $h$ ,  $\Omega_b h^2$ ,  $\Omega_m h^2$ ,  $\Omega_{\text{tot}}$ , and  $\tau$ . One can add additional parameters to this list, particularly when using the CMB in combination with other data sets. The next most relevant ones might be:  $\Omega_\nu h^2$ , the massive neutrino contribution;  $w$  ( $\equiv p/\rho$ ), the equation of state parameter for the Dark Energy; and  $dn/d\ln k$ , measuring deviations from a constant spectral index. To these 11 one could of course add further parameters describing additional physics, such as details of the reionization process, features in the initial power spectrum, a sub-dominant contribution of isocurvature modes, *etc.*

As well as these underlying parameters, there are other quantities that can be obtained from them. Such derived parameters include the actual  $\Omega$ s of the various components (*e.g.*,  $\Omega_m$ ), the variance of density perturbations at particular scales (*e.g.*,  $\sigma_8$ ), the age of the Universe today ( $t_0$ ), the age of the Universe at recombination, reionization, *etc.*

### 23.4. Physics of Anisotropies

The cosmological parameters affect the anisotropies through the well understood physics of the evolution of linear perturbations within a background FRW cosmology. There are very effective, fast, and publicly-available software codes for computing the CMB anisotropy, polarization, and matter power spectra, *e.g.*, CMBFAST [20] and CAMB [21]. These have been tested over a wide range of cosmological parameters and are considered to be accurate to better than the 1% level [22].

A description of the physics underlying the  $C_\ell$ s can be separated into 3 main regions, as shown in Fig. 23.1.

#### 23.4.1. The ISW rise, $\ell \lesssim 10$ , and Sachs-Wolfe plateau, $10 \lesssim \ell \lesssim 100$ :

The horizon scale (or more precisely, the angle subtended by the Hubble radius) at last scattering corresponds to  $\ell \simeq 100$ . Anisotropies at larger scales have not evolved significantly, and hence directly reflect the ‘initial conditions’.  $\delta T/T = -(1/5)\mathcal{R}(\mathbf{x}_{\text{LSS}}) \simeq (1/3)\delta\phi/c^2$ , here  $\delta\phi$  is the perturbation to the gravitational potential, evaluated on the last scattering surface (LSS). This is a result of the combination of gravitational redshift and intrinsic temperature fluctuations and is usually referred to as the ‘Sachs-Wolfe’ effect [23].

Assuming that a nearly scale-invariant spectrum of curvature and corresponding density perturbations was laid down at early times (*i.e.*,  $n \simeq 1$ , meaning equal power per decade in  $k$ ), then  $\ell(\ell+1)C_\ell \simeq \text{constant}$  at low  $\ell$ s. This effect is hard to see unless the multipole axis is plotted logarithmically (as in Fig. 23.1, but not Fig. 23.2).

Time variation of the potentials (*i.e.*, time-dependent metric perturbations) leads to an upturn in the  $C_\ell$ s in the lowest several multipoles; any deviation from a total equation of state  $w = 0$  has such an effect. So the dominance of the Dark Energy at low redshift makes the lowest  $\ell$ s rise above the plateau. This is sometimes called the ‘integrated Sachs-Wolfe effect’ (or ISW rise), since it comes from the line integral of  $\dot{\phi}$ ; it has been confirmed through correlations between the large-angle anisotropies and large-scale structure [24]. Specific models can also give additional contributions at low  $\ell$  (*e.g.*, perturbations in the Dark Energy component itself [25]), but typically these are buried in the cosmic variance.

In principle, the mechanism that produces primordial perturbations could generate scalar, vector, and tensor modes. However, the vector (vorticity) modes decay with the expansion of the Universe. The tensors (transverse trace-free perturbations to the metric) generate temperature anisotropies through the integrated effect of the locally anisotropic expansion of space. Since the tensor modes also redshift away after they enter the horizon, they contribute only to angular scales above about  $1^\circ$  (see Fig. 23.1). Hence some fraction of the low  $\ell$  signal could be due to a gravitational wave contribution, although small amounts of tensors are essentially impossible to discriminate from other effects that might raise the level of the plateau. However, the tensors *can* be distinguished using polarization information (see Sec. 23.6).

#### 23.4.2. The acoustic peaks, $100 \lesssim \ell \lesssim 1000$ :

On sub-degree scales, the rich structure in the anisotropy spectrum is the consequence of gravity-driven acoustic oscillations occurring before the atoms in the Universe became neutral. Perturbations inside the horizon at last scattering have been able to evolve causally and produce anisotropy at the last scattering epoch, which reflects this evolution. The frozen-in phases of these sound waves imprint a dependence on the cosmological parameters, which gives CMB anisotropies their great constraining power.

The underlying physics can be understood as follows. Before the Universe became neutral, the proton-electron plasma was tightly coupled to the photons, and these components behaved as a single ‘photon-baryon fluid.’ Perturbations in the gravitational potential, dominated by the Dark Matter component, were steadily evolving. They drove oscillations in the photon-baryon fluid, with photon pressure providing most of the restoring force and baryons giving some additional inertia. The perturbations were quite small in amplitude,  $O(10^{-5})$ , and so evolved linearly. That means each Fourier mode developed independently, and hence can be described by a driven harmonic oscillator, with frequency determined by the sound speed in

the fluid. Thus the fluid density underwent oscillations, giving time variations in temperature. These combine with a velocity effect which is  $\pi/2$  out of phase and has its amplitude reduced by the sound speed.

After the Universe recombined, the radiation decoupled from the baryons and could travel freely towards us. At that point, the phases of the oscillations were frozen-in, and became projected on the sky as a harmonic series of peaks. The main peak is the mode that went through  $1/4$  of a period, reaching maximal compression. The even peaks are maximal *under*-densities, which are generally of smaller amplitude because the rebound has to fight against the baryon inertia. The troughs, which do not extend to zero power, are partially filled by the Doppler effect because they are at the velocity maxima.

The physical length scale associated with the peaks is the sound horizon at last scattering, which can be straightforwardly calculated. This length is projected onto the sky, leading to an angular scale that depends on the geometry of space, as well as the distance to last scattering. Hence the angular position of the peaks is a sensitive probe of the spatial curvature of the Universe (*i.e.*,  $\Omega_{\text{tot}}$ ), with the peaks lying at higher  $\ell$  in open universes and lower  $\ell$  in closed geometry.

One additional effect arises from reionization at redshift  $z_i$ . A fraction of photons ( $\tau$ ) will be isotropically scattered at  $z < z_i$ , partially erasing the anisotropies at angular scales smaller than those subtended by the Hubble radius at  $z_i$ . This corresponds typically to  $\ell$ s above about a few 10s, depending on the specific reionization model. The acoustic peaks are therefore reduced by a factor  $e^{-2\tau}$  relative to the plateau.

These peaks were a clear theoretical prediction going back to about 1970 [26]. One can think of them as a snapshot of stochastic standing waves. Since the physics governing them is simple and their structure rich, then one can see how they encode extractable information about the cosmological parameters. Their empirical existence started to become clear around 1994 [27], and the emergence, over the following decade, of a coherent series of acoustic peaks and troughs is a triumph of modern cosmology. This picture has received further confirmation with the detection in the power spectrum of galaxies (at redshifts close to zero) of the imprint of these same acoustic oscillations in the baryon component [28,29,30].

#### 23.4.3. The damping tail, $\ell \gtrsim 1000$ :

The recombination process is not instantaneous, giving a thickness to the last scattering surface. This leads to a damping of the anisotropies at the highest  $\ell$ s, corresponding to scales smaller than that subtended by this thickness. One can also think of the photon-baryon fluid as having imperfect coupling, so that there is diffusion between the two components, and hence the amplitudes of the oscillations decrease with time. These effects lead to a damping of the  $C_\ell$ s, sometimes called Silk damping [31], which cuts off the anisotropies at multipoles above about 2000.

An extra effect at high  $\ell$ s comes from gravitational lensing, caused mainly by non-linear structures at low redshift. The  $C_\ell$ s are convolved with a smoothing function in a calculable way, partially flattening the peaks, generating a power-law tail at the highest multipoles, and complicating the polarization signal [32]. The effects of lensing on the CMB have recently been detected by correlating temperature gradients and small-scale filtered anisotropies from WMAP with lensing potentials traced using galaxies [33]. This is an example of a ‘secondary effect,’ *i.e.*, the processing of anisotropies due to relatively nearby structures (see Sec. 23.7.2). Galaxies and clusters of galaxies give several such effects; all are expected to be of low amplitude and typically affect only the highest  $\ell$ s, but they carry additional cosmological information and will be increasingly important as experiments push to higher sensitivity and angular resolution.

### 23.5. Current Anisotropy Data

There has been a steady improvement in the quality of CMB data that has led to the development of the present-day cosmological model. Probably the most robust constraints currently available come from the combination of the WMAP five year data [34] with smaller scale results from the ACBAR [35] and QUAD [36] experiments (together with constraints from other cosmological data-sets). We plot power spectrum estimates from these experiments, as well as BOOMERANG [38] and CBI [39] in Fig. 23.2. Other recent

experiments also give powerful constraints, which are quite consistent with what we describe below. There have been some comparisons among data-sets [37,41], which indicate very good agreement, both in maps and in derived power spectra (up to systematic uncertainties in the overall calibration for some experiments). This makes it clear that systematic effects are largely under control. However, a fully self-consistent joint analysis of all the current data sets has not been attempted, one of the reasons being that it requires a careful treatment of the overlapping sky coverage.

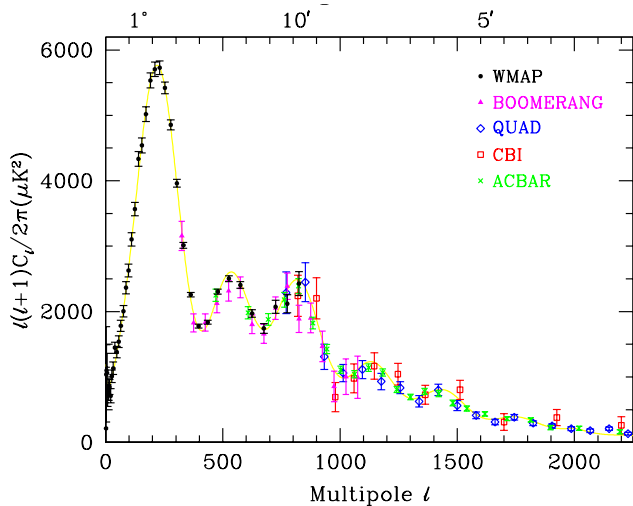


**Figure 23.2:** Band-power estimates from the WMAP, BOOMERANG, QUAD, CBI, and ACBAR experiments. Some of the low- $\ell$  and high- $\ell$  band-powers which have large error bars have been omitted. Note also that the widths of the  $\ell$ -bands varies between experiments and have not been plotted. This figure represent only a selection of available experimental results, with some other data-sets being of similar quality. The multipole axis here is linear, so the Sachs-Wolfe plateau is hard to see. However, the acoustic peaks and damping region are very clearly observed, with no need for a theoretical curve to guide the eye; the curve plotted is a best-fit model from WMAP 5-year plus other CMB data.

The band-powers shown in Fig. 23.2 are in very good agreement with a ‘ $\Lambda$ CDM’ type model, as described earlier, with several of the peaks and troughs quite apparent. For details of how these estimates were arrived at, the strength of any correlations between band-powers and other information required to properly interpret them, the original papers should be consulted.

### 23.6. CMB Polarization

Since Thomson scattering of an anisotropic radiation field also generates linear polarization, the CMB is predicted to be polarized at the roughly 5% level of the temperature anisotropies [42]. Polarization is a spin-2 field on the sky, and the algebra of the modes in  $\ell$ -space is strongly analogous to spin-orbit coupling in quantum mechanics [43]. The linear polarization pattern can be decomposed in a number of ways, with two quantities required for each pixel in a map, often given as the  $Q$  and  $U$  Stokes parameters. However, the most intuitive and physical decomposition is a geometrical one, splitting the polarization pattern into a part that comes from a divergence (often referred to as the ‘E-mode’) and a part with a curl (called the ‘B-mode’) [44]. More explicitly, the modes are defined in terms of second derivatives of the polarization amplitude, with the Hessian for the E-modes having principle axes in the same sense as the polarization, while the B-mode pattern can be thought of simply as a  $45^\circ$  rotation of the E-mode pattern. Globally one sees that the E-modes have  $(-1)^\ell$  parity (like the spherical harmonics), while the B-modes have  $(-1)^{\ell+1}$  parity.

The existence of this linear polarization allows for 6 different cross power spectra to be determined from data that measure the full temperature and polarization anisotropy information. Parity

considerations make 2 of these zero, and we are left with 4 potential observables:  $C_\ell^{\text{TT}}$ ,  $C_\ell^{\text{TE}}$ ,  $C_\ell^{\text{EE}}$ , and  $C_\ell^{\text{BB}}$ . Because scalar perturbations have no handedness, the B-mode power spectrum can only be sourced by vectors or tensors. Moreover, since inflationary scalar perturbations give only E-modes, while tensors generate roughly equal amounts of E- and B-modes, then the determination of a non-zero B-mode signal is a way to measure the gravitational wave contribution (and thus potentially derive the energy scale of inflation), even if it is rather weak. However, one must first eliminate the foreground contributions and other systematic effects down to very low levels.

The oscillating photon-baryon fluid also results in a series of acoustic peaks in the polarization  $C_\ell$ s. The main ‘EE’ power spectrum has peaks that are out of phase with those in the ‘TT’ spectrum, because the polarization anisotropies are sourced by the fluid velocity. The ‘TE’ part of the polarization and temperature patterns comes from correlations between density and velocity perturbations on the last scattering surface, which can be both positive and negative, and is of larger amplitude than the EE signal. There is no polarization ‘Sachs-Wolfe’ effect, and hence no large-angle plateau. However, scattering during a recent period of reionization can create a polarization ‘bump’ at large angular scales.

Because the polarization anisotropies have only a fraction of the amplitude of the temperature anisotropies, they took longer to detect. The first measurement of a polarization signal came in 2002 from the DASI experiment [45], which provided a convincing detection, confirming the general paradigm, but of low enough significance that it lent little constraint to models. As well as the E-mode signal, DASI also made a statistical detection of the TE correlation.

In 2003, the WMAP experiment demonstrated that it was able to measure the TE cross-correlation power spectrum with high precision [46], and this was improved upon in the 3- and 5-year results, which also included EE measurements [34,47]. The TE signal has been mapped out quite accurately now through a combination of data from WMAP, together with the BOOMERANG [54], QUAD [37], CBI [51], DASI [52] and BICEP [49,50] experiments, which are shown in Fig. 23.3. The anti-correlation at  $\ell \simeq 150$  and the peak at  $\ell \simeq 300$  are now quite distinct. The measured shape of the cross-correlation power spectrum provides supporting evidence for the adiabatic nature of the perturbations, as well as directly constraining the thickness of the last scattering surface. Since the polarization anisotropies are generated in this scattering surface, the existence of correlations at angles above about a degree demonstrates that there were super-Hubble fluctuations at the recombination epoch. The sign of this correlation also confirms the adiabatic paradigm.

Experimental band-powers for  $C_\ell^{\text{EE}}$  from WMAP plus CAPMAP [48], CBI [51], DASI [52], BOOMERANG [53], QUAD [37] and BICEP [50] are shown in Fig. 23.4. Without the benefit of correlating with the temperature anisotropies (*i.e.*, measuring  $C_\ell^{\text{TE}}$ ), the polarization anisotropies are very weak and challenging to measure. Nevertheless, there is a highly significant overall detection which is consistent with expectation. The QUAD data convincingly show the peak at  $\ell \simeq 400$  (corresponding to the first trough in  $C_\ell^{\text{TT}}$ ) and the generally oscillatory structure, while the new BICEP data show the lower peak at  $\ell \simeq 140$ .

Several experiments have reported upper limits on  $C_\ell^{\text{BB}}$ , but they are currently not very constraining. This situation should change as increasingly ambitious experiments report results.

The most distinctive result from the polarization measurements is at the largest angular scales ( $\ell < 10$ ) in  $C_\ell^{\text{TE}}$ , where there is an excess signal compared to that expected from the temperature power spectrum alone. This is precisely the signal anticipated from an early period of reionization, arising from Doppler shifts during the partial scattering at  $z < z_i$ . The effect is also confirmed in the WMAP  $C_\ell^{\text{EE}}$  results at  $\ell = 2-6$ . The amplitude of the signal indicates that the first stars, presumably the source of the ionizing radiation, formed around  $z \simeq 10$  (somewhat lower than the value suggested by the first year WMAP results, although the uncertainty is still quite large). Since this corresponds to scattering optical depth  $\tau \simeq 0.1$ , then roughly 10% of CMB photons were rescattered at the reionization epoch, with the other 90% last scattering at  $z \simeq 1100$ .

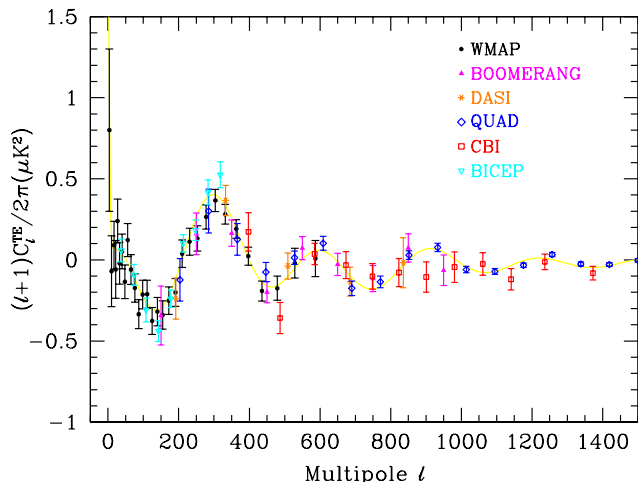


**Figure 23.3:** Cross power spectrum of the temperature anisotropies and E-mode polarization signal from WMAP [47], together with estimates from BOOMERANG, DASI, QUAD, CBI and BICEP, several of which extend to higher  $\ell$ . Note that the widths of the bands have been suppressed for clarity, but that in some cases they are almost as wide as the features in the power spectrum. Also note that the  $y$ -axis here is not multiplied by the additional  $\ell$ , which helps to show both the large and small angular scale features.

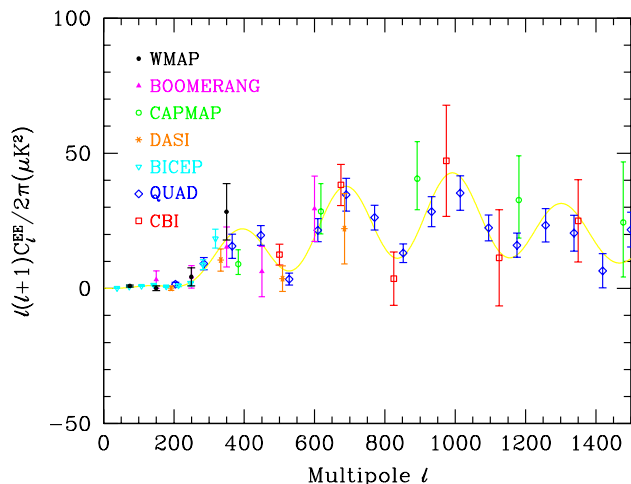


**Figure 23.4:** Power spectrum of E-mode polarization from several different experiments, plotted along with a theoretical model which fits WMAP plus other CMB data.

## 23.7. Complications

There are a number of issues which complicate the interpretation of CMB anisotropy data (and are considered to be *signal* by many astrophysicists), some of which we sketch out below.

### 23.7.1. Foregrounds :

The microwave sky contains significant emission from our Galaxy and from extra-galactic sources [55]. Fortunately, the frequency dependence of these various sources is in general substantially different from that of the CMB anisotropy signals. The combination of Galactic synchrotron, bremsstrahlung, and dust emission reaches a minimum at a wavelength of roughly 3 mm (or about 100 GHz). As one moves to greater angular resolution, the minimum moves to slightly higher frequencies, but becomes more sensitive to unresolved (point-like) sources.

At frequencies around 100 GHz, and for portions of the sky away from the Galactic Plane, the foregrounds are typically 1 to 10% of the CMB anisotropies. By making observations at multiple frequencies, it is relatively straightforward to separate the various components and determine the CMB signal to the few per cent level. For greater

sensitivity, it is necessary to use the spatial information and statistical properties of the foregrounds to separate them from the CMB.

The foregrounds for CMB polarization are expected to follow a similar pattern, but are less well studied, and are intrinsically more complicated. The three year WMAP data have shown that the polarized foregrounds dominate at large angular scales, and that they must be well characterized in order to be discriminated [56]. Whether it is possible to achieve sufficient separation to detect B-mode CMB polarization is still an open question. However, for the time being, foreground contamination is not a fundamental limit for CMB experiments.

### 23.7.2. Secondary Anisotropies :

With increasingly precise measurements of the primary anisotropies, there is growing theoretical and experimental interest in ‘secondary anisotropies,’ pushing experiments to higher angular resolution and sensitivity. These secondary effects arise from the processing of the CMB due to ionization history and the evolution of structure, including gravitational lensing and patchy reionization effects [57]. Additional information can thus be extracted about the Universe at  $z \ll 1000$ . This tends to be most effectively done through correlating CMB maps with other cosmological probes of structure. Secondary signals are also typically non-Gaussian, unlike the primary CMB anisotropies.

### 23.7.3. Sunyaev-Zel’dovich Effect :

A secondary signal of great current interest is the Sunyaev-Zel’dovich (SZ) effect [58], which is Compton scattering ( $\gamma e \rightarrow \gamma' e'$ ) of the CMB photons by hot electron gas, which creates spectral distortions by transferring energy from the electrons to the photons. It is particularly important for clusters of galaxies, through which one observes a partially Comptonized spectrum, resulting in a decrement at radio wavelengths and an increment in the submillimeter.

The imprint on the CMB sky is of the form  $\Delta T/T = y f(x)$ , with the  $y$ -parameter being the integral of Thomson optical depth times  $kT_e/m_e c^2$  through the cluster, and  $f(x)$  describing the frequency dependence. This is simply  $x \coth(x/2) - 4$  for a non-relativistic gas (the electron temperature in a cluster is typically a few keV), where the dimensionless frequency  $x \equiv h\nu/kT_\gamma$ . As well as this ‘thermal’ SZ effect, there is also a smaller ‘kinetic’ effect due to the bulk motion of the cluster gas, this being  $\Delta T/T \sim \tau(v/c)$ , with either sign, but having the same spectrum as the primary CMB anisotropies.

A significant advantage in finding galaxy clusters this way is that the SZ effect is largely independent of redshift, so in principle clusters can be found to arbitrarily large distances. The SZ effect can be used to find and study individual clusters, and to obtain estimates of the Hubble constant. There is also the potential to constrain the equation of state of the Dark Energy through counts of detected clusters as a function of redshift [59]. Many experiments (including the *Planck* satellite) are currently in operation which will probe clusters in this way. The promise of the method has been realised through the first detections of clusters purely through the SZ effect, by the SPT [60] and ACT [61] experiments.

### 23.7.4. Higher-order Statistics :

Although most of the CMB anisotropy information is contained in the power spectra, there will also be weak signals present in higher-order statistics. These statistics can measure any primordial non-Gaussianity in the perturbations, as well as non-linear growth of the fluctuations on small scales and other secondary effects (plus residual foreground contamination of course). Although there are an infinite variety of ways in which the CMB could be non-Gaussian, there is a generic form to consider for the initial conditions, where a quadratic contribution to the curvature perturbations is parameterized through a dimensionless number  $f_{\text{NL}}$ . This weakly non-linear component can be constrained through measurements of the bispectrum or Minkowski functionals, for example. The constraints depend on the shape of the triangles in harmonic space, and it has become common to distinguish the ‘local’ or ‘squeezed’ configuration (in which one side is much smaller than the other two) from the ‘equilateral’ configuration. The results from the WMAP team are  $-9 < f_{\text{NL}} < 111$  (95% confidence region), for the local mode and  $-151 < f_{\text{NL}} < 253$  for the equilateral mode [14]. Different estimators used by other authors give results of similar magnitude [62].

The level of  $f_{\text{NL}}$  expected is small, so that a detection of  $f_{\text{NL}} \gtrsim 10$  would rule out all single field, slow-roll inflationary models. However, with the capabilities of *Planck* and other future experiments, it seems that a measurement of primordial non-Gaussianity may be feasible for a wide class of models, and therefore much effort is expected to be devoted to predictions and measurements in the coming years.

### 23.8. Constraints on Cosmologies

The most striking outcome of the newer experimental results is that the standard cosmological paradigm is in very good shape. A large amount of high precision data on the power spectrum is adequately fit with fewer than 10 free parameters. The framework is that of FRW models, which have nearly flat geometry, containing Dark Matter and Dark Energy, and with adiabatic perturbations having close to scale invariant initial conditions.

Within this framework, bounds can be placed on the values of the cosmological parameters. Of course, much more stringent constraints can be placed on models which cover a restricted parameter space, *e.g.*, assuming that  $\Omega_{\text{tot}} = 1$ ,  $n = 1$  or  $r = 0$ . More generally, the constraints depend upon the adopted prior probability distributions, even if they are implicit, for example by restricting the parameter freedom or their ranges (particularly where likelihoods peak near the boundaries), or by using different choices of other data in combination with the CMB. When the data become even more precise, these considerations will be less important, but for now we caution that restrictions on model space and choice of priors need to be kept in mind when adopting specific parameter values and uncertainties.

There are some combinations of parameters that fit the CMB anisotropies almost equivalently. For example, there is a nearly exact geometric degeneracy, where any combination of  $\Omega_{\text{m}}$  and  $\Omega_{\Lambda}$  that gives the same angular diameter distance to last scattering will give nearly identical  $C_{\ell}$ s. There are also other less exact degeneracies among the parameters. Such degeneracies can be broken when using the CMB results in combination with other cosmological data sets. Particularly useful are complementary constraints from galaxy clustering, the abundance of galaxy clusters, baryon acoustic oscillations, weak gravitational lensing measurements, Type Ia supernova distances, and the distribution of Lyman  $\alpha$  forest clouds. For an overview of some of these other cosmological constraints, see The Cosmological Parameters—Sec. 21 of this *Review*.

The 5-year *WMAP* data alone, together with constraints from Hubble constant determination [63], supernovae [64] and baryon acoustic oscillations [29], within the context of a 6 parameter family of models (which fixes  $\Omega_{\text{tot}} = 1$  and  $r = 0$ ), yield the following results [14]:  $A = (2.44 \pm 0.10) \times 10^{-9}$ ,  $n = 0.960 \pm 0.013$ ,  $h = 0.705 \pm 0.013$ ,  $\Omega_{\text{b}}h^2 = 0.0227 \pm 0.0006$ ,  $\Omega_{\text{m}}h^2 = 0.136 \pm 0.004$  and  $\tau = 0.084 \pm 0.016$ . There has been little substantive change compared with the 3-year data, although the error bars are reduced with more integration time and the inclusion of lower frequency polarization data. The better measurement of the third acoustic peak, together with improved understanding of calibration issues has led to tighter error bars on dark matter density and overall normalization. The evidence for non-zero reionization optical depth is now very compelling, while the evidence for  $n < 1$  is still only at the roughly  $3\sigma$  level.

Other combinations of data, *e.g.*, including additional CMB measurements, or using cosmological constraints, lead to consistent results to those given above, sometimes with smaller error bars, and with the precise values depending on data selection [30,37,65]. Note that for  $h$ , the CMB data alone provide only a very weak constraint, unless spatial flatness or some other cosmological data are used. For  $\Omega_{\text{b}}h^2$ , the precise value depends sensitively on how much freedom is allowed in the shape of the primordial power spectrum (see Big-Bang nucleosynthesis—Sec. 20 of this *Review*). The addition of other data-sets also allows for constraints to be placed on further parameters.

For  $\Omega_{\text{tot}}$ , perhaps the best *WMAP* constraint is  $1.006 \pm 0.006$ , from the combination with supernova and baryon acoustic oscillation constraints (and setting  $w = -1$ ). The 95% confidence upper limit on  $r$  is 0.43 using *WMAP* alone, tightening to  $r < 0.22$  with the addition of other data [14]. This limit depends on how the slope  $n$  is restricted and whether  $dn/d\ln k \neq 0$  is allowed. Nevertheless, it is clear that  $\lambda\phi^4$  (sometimes called self-coupled) inflation is disfavored

by the data, while the  $m^2\phi^2$  (sometimes called mass term) inflationary model is still allowed [14]. Gravity wave constraints coming directly from B-mode limits are at the level of  $r < 0.73$  [50].

There are also constraints on parameters over and above the basic 8 that we have described, usually requiring extra cosmological data to break degeneracies. For example, the addition of the Dark Energy equation of state  $w$  adds the partial degeneracy of being able to fit a ridge in  $(w, h)$  space, extending to low values of both parameters. This degeneracy is broken when the CMB is used in combination with independent  $H_0$  limits, or other data. *WMAP* plus supernova and large-scale structure data yield  $-0.14 < 1 + w < 0.12$  (95% confidence), with stronger constraints for flat models.

For the optical depth  $\tau$ , the best-fit corresponds to a reionization redshift centered on 11 in the best-fit cosmology, and assuming instantaneous reionization. This redshift appears to be higher than that suggested from studies of absorption in high- $z$  quasar spectra [66]. The excitement here is that we have direct information from CMB polarization which can be combined with other astrophysical measurements to understand when the first stars formed and brought about the end of the cosmic dark ages.

### 23.9. Particle Physics Constraints

CMB data are beginning to put limits on parameters which are directly relevant for particle physics models. For example, there is a limit on the neutrino contribution  $\Omega_{\nu}h^2 < 0.0071$  (95% confidence) from a combination of *WMAP* and other data [14]. This directly implies a limit on neutrino mass,  $\sum m_{\nu} < 0.67$  eV, assuming the usual number density of fermions which decoupled when they were relativistic. Some tighter constraints can be derived using the CMB in combination with other data-sets [67].

The current suite of data suggest that  $n < 1$ , with a best-fitting value about 5% below unity. If borne out, this would be quite constraining for inflationary models. Moreover, this gives a real target for B-mode searches, since the value of  $r$  in simple models may be in the range of detectability, *e.g.*,  $r \sim 0.2$  for  $m^2\phi^2$  inflation if  $n \simeq 0.95$ . In addition, a combination of the *WMAP* data with other data-sets constrains the running of the spectral index, although at the moment there is no evidence for  $dn/d\ln k \neq 0$  [14].

One other hint of new physics lies in the fact that the quadrupole and possibly some of the other low  $\ell$  modes seem anomalously low compared with the best-fit  $\Lambda$ CDM model [6]. Additionally there is some weak evidence for a large scale modulation of the smaller-scale power [16]. These effects might be expected in a universe which has a large-scale cut-off or anisotropy in the initial power spectrum, or is topologically non-trivial. However, cosmic variance, possible foregrounds, apparent correlations between modes (as mentioned in Sec. 23.2), *etc.*, limit the significance of these anomalies.

In addition, it is also possible to put limits on other pieces of physics [68], for example the neutrino chemical potentials, contribution of Warm Dark Matter, decaying particles, time variation of the fine-structure constant, or physics beyond general relativity. Further particle physics constraints will follow as the anisotropy measurements increase in precision.

Careful measurement of the CMB power spectra and non-Gaussianity can in principle put constraints on physics at the highest energies, including ideas of string theory, extra dimensions, colliding branes, *etc.* At the moment any calculation of predictions appears to be far from definitive. However, there is a great deal of activity on implications of string theory for the early Universe, and hence a very real chance that there might be observational implications for specific scenarios.

### 23.10. Fundamental Lessons

More important than the precise values of parameters is what we have learned about the general features which describe our observable Universe. Beyond the basic hot Big Bang picture, the CMB has taught us that:

- The Universe recombined at  $z \simeq 1100$  and started to become ionized again at  $z \simeq 10$ .
- The geometry of the Universe is close to flat.

- Both Dark Matter and Dark Energy are required.
- Gravitational instability is sufficient to grow all of the observed large structures in the Universe.
- Topological defects were not important for structure formation.
- There are ‘synchronized’ super-Hubble modes generated in the early Universe.
- The initial perturbations were adiabatic in nature.
- The perturbations had close to Gaussian (*i.e.*, maximally random) initial conditions.

It is very tempting to make an analogy between the status of the cosmological ‘Standard Model’ and that of particle physics (see earlier Sections of this *Review*). In cosmology there are about 10 free parameters, each of which is becoming well determined, and with a great deal of consistency between different measurements. However, none of these parameters can be calculated from a fundamental theory, and so hints of the bigger picture, ‘physics beyond the Standard Model,’ are being searched for with ever more ambitious experiments.

Despite this analogy, there are some basic differences. For one thing, many of the cosmological parameters change with cosmic epoch, and so the measured values are simply the ones determined today, and hence they are not ‘constants,’ like particle masses for example (although they *are* deterministic, so that if one knows their values at one epoch, they can be calculated at another). Moreover, the number of parameters is not as fixed as it is in the particle physics Standard Model; different researchers will not necessarily agree on what the free parameters are, and new ones can be added as the quality of the data improves. In addition, parameters like  $\tau$ , which come from astrophysics, are in principle calculable from known physical processes. On top of all this, other parameters might be ‘stochastic’ in that they may be fixed only in our observable patch of the Universe or among certain vacuum states in the ‘Landscape’ [70].

In a more general sense, the cosmological ‘Standard Model’ is much further from the underlying ‘fundamental theory,’ which will ultimately provide the values of the parameters from first principles. Nevertheless, any genuinely complete ‘theory of everything’ must include an explanation for the values of these cosmological parameters as well as the parameters of the Standard Model of particle physics.

### 23.11. Future Directions

Given the significant progress in measuring the CMB sky, which has been instrumental in tying down cosmological parameters, what can we anticipate for the future? There will be a steady improvement in the precision and confidence with which we can determine the appropriate cosmological model and its parameters. Ground-based experiments operating at smaller angular scales will over the next few years provide significantly tighter constraints on the damping tail. New polarization experiments will continue to push down the constraints on primordial B-modes. The third generation CMB satellite mission, *Planck* was launched successfully in May 2009, and the first results are keenly anticipated.

Despite the increasing improvement in the results, the addition of the latest experiments has not significantly changed the established cosmological model. It is, therefore, appropriate to ask: what should we expect to come from *Planck* and from other future experiments, including those being discussed in the U.S. and in Europe? *Planck* certainly has the advantage of high sensitivity and a full-sky survey. A precise measurement of the third acoustic peak provides a good determination of the matter density; this can only be done by measurements which are accurate relative to the first two peaks (which themselves constrain the curvature and the baryon density). A detailed measurement of the damping tail region will also significantly improve the determination of  $n$  and any running of the slope. *Planck* should be capable of measuring  $C_\ell^{\text{EE}}$  quite well, providing both a strong check on the cosmological Standard Model and extra constraints that will improve parameter estimation.

A set of cosmological parameters is now known to roughly 10% accuracy, and that may seem sufficient for many people. However, we should certainly demand more of measurements which describe *the entire observable Universe!* Hence a lot of activity in the coming years will continue to focus on determining those parameters with increasing precision. This necessarily includes testing for consistency

among different predictions of the cosmological Standard Model, and searching for signals which might require additional physics.

A second area of focus will be the smaller scale anisotropies and ‘secondary effects.’ There is a great deal of information about structure formation at  $z \ll 1000$  encoded in the CMB sky. This may involve higher-order statistics as well as spectral signatures, with many new experiments targeting the galaxy cluster SZ effect. Such investigations can also provide constraints on the Dark Energy equation of state, for example. *Planck*, as well as new telescopes aimed at the highest  $\ell$ s, should be able to make a lot of progress in this arena.

A third direction is increasingly sensitive searches for specific signatures of physics at the highest energies. The most promising of these may be the primordial gravitational wave signals in  $C_\ell^{\text{BB}}$ , which could be a probe of the  $\sim 10^{16}$  GeV energy range. As well as *Planck*, there are several ground- and balloon-based experiments underway which are designed to probe the polarization B-modes. Whether the amplitude of the effect coming from inflation will be detectable is unclear, but the prize makes the effort worthwhile, and the indications that  $n \simeq 0.95$  give some genuine optimism that  $r(= T/S)$  may be of order 0.1, and hence within reach soon.

Anisotropies in the CMB have proven to be the premier probe of cosmology and the early Universe. Theoretically the CMB involves well-understood physics in the linear regime, and is under very good calculational control. A substantial and improving set of observational data now exists. Systematics appear to be well understood and not a limiting factor. And so for the next few years we can expect an increasing amount of cosmological information to be gleaned from CMB anisotropies, with the prospect also of some genuine surprises.

### References:

1. A.A. Penzias and R. Wilson, *Astrophys. J.* **142**, 419 (1965); R.H. Dicke *et al.*, *Astrophys. J.* **142**, 414 (1965).
2. M. White, D. Scott, and J. Silk, *Ann. Rev. Astron. & Astrophys.* **32**, 329 (1994); W. Hu and S. Dodelson, *Ann. Rev. Astron. & Astrophys.* **40**, 171 (2002).
3. G.F. Smoot *et al.*, *Astrophys. J.* **396**, L1 (1992).
4. C.L. Bennett *et al.*, *Astrophys. J. Supp.* **148**, 1 (2003).
5. N. Jarosik *et al.*, *Astrophys. J. Supp.* **170**, 263 (2007).
6. G. Hinshaw *et al.*, *Astrophys. J. Supp.* **180**, 225 (2009).
7. J.C. Mather *et al.*, *Astrophys. J.* **512**, 511 (1999).
8. D.J. Fixsen *et al.*, [arXiv:0901.0555](https://arxiv.org/abs/0901.0555).
9. S. Courteau *et al.*, *Astrophys. J.* **544**, 636 (2000).
10. D.J. Fixsen *et al.*, *Astrophys. J.* **420**, 445 (1994).
11. D.J. Fixsen *et al.*, *Astrophys. J.* **473**, 576 (1996); A. Kogut *et al.*, *Astrophys. J.* **419**, 1 (1993).
12. S. Seager, D.D. Sasselov, and D. Scott, *Astrophys. J. Supp.* **128**, 407 (2000).
13. N. Bartolo *et al.*, *Phys. Rep.* **402**, 103 (2004).
14. E. Komatsu *et al.*, *Astrophys. J. Supp.* **180**, 330 (2009).
15. A. de Oliveira-Costa *et al.*, *Phys. Rev.* **D69**, 063516 (2004); J.D. McEwen *et al.*, *Monthly Not. Royal Astron. Soc.* **388**, 659 (2008).
16. J. Hoftuft *et al.*, *Astrophys. J.* **699**, 985 (2009).
17. L. Knox, *Phys. Rev.* **D52**, 4307 (1995).
18. I. Sollom, A. Challinor, and M.P. Hobson, *Phys. Rev.* **D79**, 123521 (2009).
19. A.R. Liddle and D.H. Lyth, *Cosmological Inflation and Large-Scale Structure*, Cambridge University Press (2000).
20. U. Seljak and M. Zaldarriaga, *Astrophys. J.* **469**, 437 (1996).
21. A. Lewis, A. Challinor, and A. Lasenby, *Astrophys. J.* **538**, 473 (2000).
22. U. Seljak *et al.*, *Phys. Rev.* **D68**, 083507 (2003).
23. R.K. Sachs and A.M. Wolfe, *Astrophys. J.* **147**, 73 (1967).
24. R. Crittenden and N. Turok, *Phys. Rev. Lett.* **76**, 575 (1996); T. Giannantonio *et al.*, *Phys. Rev.* **D77**, 123520 (2008); S. Ho *et al.*, *Phys. Rev.* **D78**, 043519 (2008).
25. W. Hu and D.J. Eisenstein, *Phys. Rev.* **D59**, 083509 (1999); W. Hu *et al.*, *Phys. Rev.* **D59**, 023512 (1999).

26. P.J.E. Peebles and J.T. Yu, *Astrophys. J.* **162**, 815 (1970);  
R.A. Sunyaev and Ya.B. Zel'dovich, *Astrophys. & Space Sci.* **7**,  
3 (1970).
27. D. Scott, J. Silk, and M. White, *Science* **268**, 829 (1995).
28. D.J. Eisenstein *et al.*, *Astrophys. J.* **633**, 560 (2005).
29. W.J. Percival *et al.*, *Monthly Not. Royal Astron. Soc.* **381**, 1053  
(2007).
30. W.J. Percival *et al.*, [arXiv:0907.1660](#).
31. J. Silk, *Astrophys. J.* **151**, 459 (1968).
32. M. Zaldarriaga and U. Seljak, *Phys. Rev.* **D58**, 023003 (1998);  
A. Lewis and A. Challinor, *Phys. Rep.* **429**, 1 (2006).
33. K.M. Smith, O. Zahn, and O. Doré, *Phys. Rev.* **D76**, 3510  
(2007);  
C.M. Hirata *et al.*, *Phys. Rev.* **D78**, 043520 (2008).
34. M.R. Nolta *et al.*, *Astrophys. J. Supp.* **180**, 296 (2009).
35. M.C. Runyan *et al.*, *Astrophys. J. Supp.* **149**, 265 (2003);  
C.L. Reichardt *et al.*, *Astrophys. J.* **694**, 1200 (2009).
36. J.R. Hinderks *et al.*, *Astrophys. J.* **692**, 1221 (2009);  
R.B. Friedman *et al.*, *Astrophys. J.* **700**, L187 (2009).
37. M.L. Brown *et al.*, [arXiv:0906.1003](#).
38. S. Masi *et al.*, *Astron. & Astrophys.* **458**, 687 (2006);  
W.C. Jones *et al.*, *Astrophys. J.* **647**, 823 (2006).
39. S. Padin *et al.*, *Publ. Astron. Soc. Pacific* **114**, 83 (2002);  
J.L. Sievers *et al.*, [arXiv:0901.4540](#).
40. N.W. Halverson *et al.*, *Astrophys. J.* **568**, 38 (2002).
41. M.E. Abroe *et al.*, *Astrophys. J.* **605**, 607 (2004);  
N. Rajguru *et al.*, *Monthly Not. Royal Astron. Soc.* **363**, 1125  
(2005).
42. W. Hu and M. White, *New Astron.* **2**, 323 (1997).
43. W. Hu and M. White, *Phys. Rev.* **D56**, 596 (1997).
44. M. Zaldarriaga and U. Seljak, *Phys. Rev.* **D55**, 1830 (1997);  
M. Kamionkowski, A. Kosowsky, and A. Stebbins, *Phys. Rev.*  
**D55**, 7368 (1997).
45. J. Kovac *et al.*, *Nature*, **420**, 772 (2002).
46. A. Kogut *et al.*, *Astrophys. J. Supp.* **148**, 161 (2003).
47. L. Page *et al.*, *Astrophys. J. Supp.* **170**, 335 (2007).
48. D. Barkats *et al.*, *Astrophys. J.* **619**, L127 (2005);  
C. Bischoff *et al.*, *Astrophys. J.* **684**, 771 (2008).
49. Y.D. Takahashi *et al.*, [arXiv:0906.4069](#).
50. H.C. Chiang *et al.*, [arXiv:0906.1181](#).
51. A.C.S. Readhead *et al.*, *Science*, **306**, 836 (2004);  
J.L. Sievers *et al.*, *Astrophys. J.* **660**, 976 (2007).
52. E.M. Leitch *et al.*, *Astrophys. J.* **624**, 10 (2005).
53. T.E. Montroy *et al.*, *Astrophys. J.* **647**, 813 (2006).
54. F. Piacentini *et al.*, *Astrophys. J.* **647**, 833 (2006).
55. A. de Oliveira-Costa, M. Tegmark (eds.), *Microwave Foregrounds*,  
*Astron. Soc. of the Pacific, San Francisco* (1999).
56. B. Gold *et al.*, *Astrophys. J. Supp.* **180**, 265 (2009).
57. N. Aghanim, S. Majumdar, and J. Silk, *Rept. Prog. Phys.*, **71**,  
066902 (2008).
58. R.A. Sunyaev and Ya.B. Zel'dovich, *Ann. Rev. Astron. Astrophys.*  
**18**, 537 (1980);  
M. Birkinshaw, *Phys. Rep.* **310**, 98 (1999).
59. J.E. Carlstrom, G.P. Holder, and E.D. Reese, *Ann. Rev. Astron.*  
*& Astrophys.* **40**, 643 (2002).
60. Z. Staniszewski *et al.*, *Astrophys. J.* **701**, 32 (2009).
61. A.D. Hincks *et al.*, [arXiv:0907.0461](#).
62. A.P.S. Yadav and D. Wandelt, *Phys. Rev. Lett.* **100**, 1301  
(2008);  
K.M. Smith, L. Senatore, and M. Zaldarriaga, [arXiv:0901.2572](#)  
.
63. W.L. Freedman *et al.*, *Astrophys. J.* **553**, 47 (2001).
64. M. Kowalski *et al.*, *Astrophys. J.* **686**, 749 (2008).
65. J. Dunkley *et al.*, *Astrophys. J. Supp.* **180**, 306 (2009).
66. X. Fan *et al.*, *Astrophys. J.* **123**, 1247 (2002).
67. U. Seljak, A. Slosar, and P. McDonald, *JCAP*, **10**, 014 (2006);  
A. Goobar *et al.*, *J. Cosm. & Astropart. Phys.* **6**, 019 (2006);  
G.L. Fogli *et al.*, *Phys. Rev.* **D75**, 053001 (2007).
68. M. Kamionkowski and A. Kosowsky, *Ann. Rev. Nucl. Part. Sci.*  
**49**, 77 (1999).
69. R. Maartens, *Living Rev. Rel.* **7**, 7 (2004).
70. R. Bousso and J. Polchinski, *JHEP* 0006, 006 (2000);  
L. Susskind, *The Davis Meeting On Cosmic Inflation* (2003),  
[hep-th/0302219](#).